

# **Ionospheric Observations from the ISS: Overcoming Noise Challenges in Signal Extraction**

Rachel Ulrich

Statistics, Computing and Artificial Intelligence Division, Los Alamos  
National Laboratory

Kelly R. Moran

Statistics, Computing and Artificial Intelligence Division, Los Alamos  
National Laboratory

Ky Potter

Statistics, Computing and Artificial Intelligence Division, Los Alamos  
National Laboratory

Statistics and Actuarial Science Department, Simon Fraser University

Lauren A. Castro

Analytics, Intelligence and Technology Division, Los Alamos National  
Laboratory

Gabriel R. Wilson

Space Science and Applications, Intelligence and Space Research  
Division, Los Alamos National Laboratory

Brian Weaver

Statistics, Computing and Artificial Intelligence Division, Los Alamos  
National Laboratory

Carlos Maldonado

Space Science and Applications, Intelligence and Space Research  
Division, Los Alamos National Laboratory

February 4, 2026

**Abstract**

The Electric Propulsion Electrostatic Analyzer Experiment (ÈPÈE) is a compact ion energy bandpass filter deployed on the International Space Station (ISS) in March 2023 and providing continuous measurements through April 2024. This period coincides with the Solar Cycle 25 maximum, capturing unique observations of solar activity extremes in the mid- to low-latitude regions of the topside ionosphere. From these in situ spectra we derive plasma parameters that inform space-weather impacts on satellite navigation and radio communication. We present a statistical processing pipeline for ÈPÈE that (i) estimates the instrument noise floor, (ii) accounts for irregular temporal sampling, and (iii) extracts ionospheric signals. Rather than discarding noisy data, the method learns a baseline noise model and fits the measurement surface using a scaled Vecchia Gaussian process approximation, recovering values typically rejected by thresholding. The resulting products increase data coverage and enable noise-assisted monitoring of ionospheric variability.

*Keywords:* Gaussian processes, Scaled Vecchia, Ionospheric science, signal processing

# 1 Introduction

## 1.1 Background on EPEE instrument

The Electric Propulsion Electrostatic Analyzer Experiment (ÈPÈE) is a low-cost, rugged, compact laminated electrostatic analyzer (ESA) deployed on the International Space Station (ISS) in March 2023. ÈPÈE provided continuous measurements from its deployment through April 2024, spanning the entry into the maximum of Solar Cycle 25 (Maldonado et al. 2025). In space plasma physics, electrostatic analyzers (ESAs) are widely used for measuring particle energy per unit charge ( $E/q$ ). By combining sensor geometry with an applied electric field to form an energy band-pass filter, ÈPÈE measures ion energy and current from local charged particle populations. (Maldonado et al. 2025, 2023). From these measurements, macroscopic parameters of interest can be derived.

The ISS orbits at approximately 400 kilometers above the Earth’s surface, providing critical measurements of the top-side ionosphere directly above the F2 peak that cannot be obtained from ground-based methods (Maldonado et al. 2025). The ionosphere is a low-density, “cold” plasma dictating that currents are relatively small (reported in nanoamperes) and

temperatures are low (0.1-0.2 electron Volts). Accurate plasma measurements facilitate understanding of the complex relationships between solar storms, the solar cycle, eclipse, and spacecraft charging. This understanding is essential not only for exploring phenomena of scientific interest (e.g., the Equatorial Ionization Anomaly and Traveling Ionospheric Disturbances), but also for anticipating space-weather effects on the growing number of low Earth orbit satellites that support navigation, communication, and national security ([Minow et al. 2024](#)).

The ÈPÈE instrument provides measurements at a rate of 0.5 Hz, resulting in a single data point approximately every two seconds. Due to the selective filter design, at each timestamp ( $t$ ) a measurement of the current (**I**) and energy (**E**) in electron Volts (eV) is recorded for each of 100 discrete energy bins (**B** with  $b = 1, 2, \dots, B$ ). Energy values are discretized into bins with the total observed range spanning approximately 0.8 - 185 eV. At each timestamp we have values of current across energy bins ( $I_{t,b}$ ), or a distribution of current that characterizes the local space plasma at that moment in time.

Interpretation of ÈPÈE's measurements relies on basic principles of plasma physics. Recalling that a plasma consists of electrons, ions, and neutrals, each species can be described by a distribution function  $f_\alpha(\mathbf{r}, \mathbf{v}, t)$  that evolves under external forces and collisions, where  $\mathbf{r}$  and  $\mathbf{v}$  are the position and velocity vectors and  $t$  is time. This function, often referred to as the *phase space density*, represents the number of particles per unit volume in real and velocity space — that is, the particle density at a given velocity, position, and time. Because individual motions cannot be observed, macroscopic parameters—such as density and temperature—are estimated by taking moments of these distributions ([Howard 2002](#)).

Due to ÈPÈE's limited field of view, the movement of space plasma relative to the detector face is primarily along the velocity vector, allowing the use of a one-dimensional Maxwellian distribution,  $f(v_x)$ , as an analytical approximation to the ion velocity distribution. Here,

$f(v_x)$  is a species-specific simplification of the general distribution  $f_\alpha(r, v, t)$ , assuming spatial and temporal homogeneity and that perpendicular velocity components contribute negligibly within EPÈE's narrow field of view. However, because the plasma cannot be considered to be in thermal equilibrium owing to external interference from the ISS, a *drifted Maxwellian* is used to account for the resulting bulk flow velocity. This distribution depends on  $n, m, k, T$  and the drift velocity  $v_{x,d}$ , where  $k$  is the Boltzmann constant,  $m, T$  are species-specific (with  $T$  representing the thermal spread in local equilibrium), and  $n$  is the total number density serving as the normalizing constant (Maldonado et al. 2023):

$$f(v_x) = n \left( \frac{m}{2\pi kT} \right)^{1/2} \exp\left( \frac{-m}{2kT} (v_x - v_{x,d})^2 \right) \quad (1)$$

The form of this distribution is familiar, as it is a special application of the Gaussian distribution.

EPÈE measures ion current arising from the flux of charged particles transmitted through its energy bandpass at each voltage step. The measured current  $I \propto q \int v_x f(v_x) dv_x$  therefore reflects the velocity distribution weighted by particle speed within the analyzer's selected energy-per-charge window. The current peak ( $I_{0,t}$ ) occurs at the most probable energy ( $E_{0,t}$ ) linking the drifted Maxwellian form of Eq. 1 to the subsequent energy relation used to infer the spacecraft potential  $\phi_t$  (Maldonado et al. 2023):

$$E_{0,t} = \frac{1}{2}mv_x^2 + q\phi_t \quad (2)$$

Thus, selecting the maximum current value ( $I_{0,t}$ ) and respective energy value ( $E_{0,t}$ ) at a given timestamp allows us to solve for spacecraft potential ( $\phi_t$ ).

Figure 1 demonstrates the distribution of current values for a single moment in time under the conditions in which a Maxwellian is a reasonable approximation. The peak current

value describes the most likely value and is matched to the energy value for the respective energy bin.

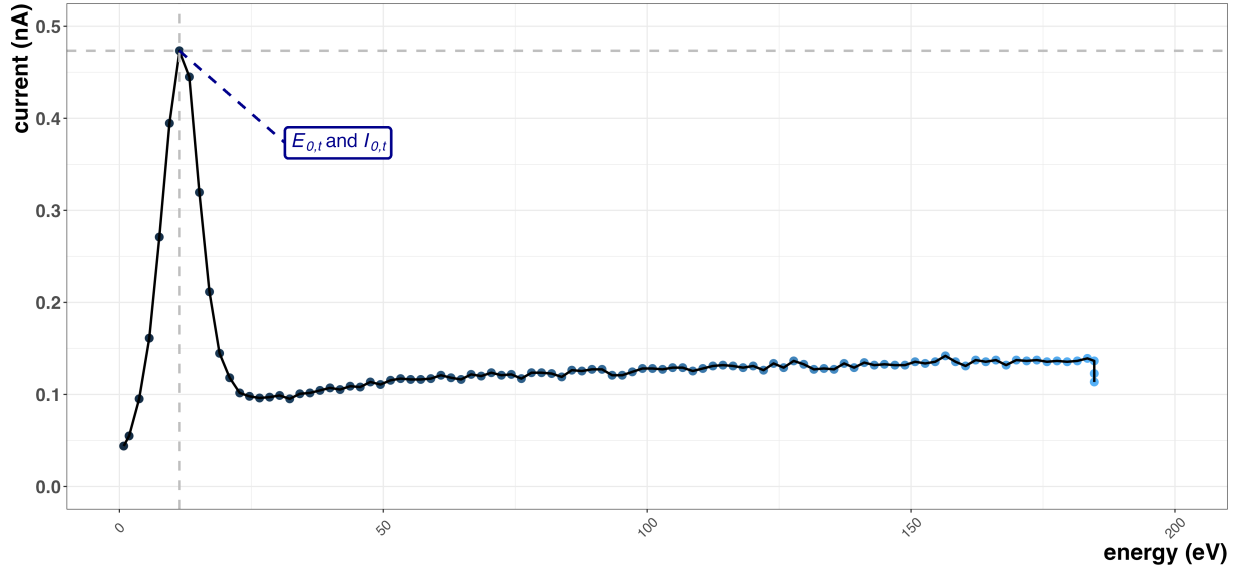


Figure 1: Distribution of current values across energy bins for a single timestamp (2023-09-29 00:33:18 UTC). Discrete current observations are marked by points and the underlying empirical distribution is fit with a line. Energy bin is on the x-axis and current is on the y-axis (nA) with color referring to energy value (eV). Energy value is discretized by bins; energy values increase as bin number increases. This is referenced with indigo blues fading to azure as energy value increases across the x-axis. Gray lines indicate the intersection of the maximum values for current and energy.

## 1.2 Background on Spacecraft Charging

The electrical charging physics of the ISS are complex. In brief, the design and motion of the ISS and interaction with the ionosphere produce conditions potentially hazardous to astronauts during extravehicular activity, and to the surface of the ISS itself (please see [Hastings \(1995\)](#) for a detailed explanation). Initially, the Floating Potential Measurement Unit (FPMU) was deployed in 2006 as a permanent diagnostic tool of charging physics,

designed with four separate instruments that together produced reliable measurements of ambient plasma density and electron temperature in addition to frame potential (Swenson et al. 2003, Minow et al. 2023).

Although intended for only three years operation, the FPMU has provided observations of local space plasma for nearly two decades (Minow et al. 2023). However, these data were not a continuous record, rendering EPEE the main provider of data for its limited lifetime deployment. A seven-hour period of overlap exists between the two data sets in 2023, on Julian days 271 and 272. This period of overlap will be used as the case example - and opportunity for comparison - for the remainder of the analysis in instances where subsets of the data record are most efficacious for visualization.

As shown in Equation (2), determining spacecraft charge at a given timestamp requires the selection of the maximum current value and respective energy value, resulting in data formatted with a single current value, energy bin, energy value and spacecraft charge value per timestamp. If, however, our assumed underlying distribution does not reasonably approximate the data, taking the maximum current value does not align with our expectation. Below, Figure 2 shows an empirical distribution of current values for a single timestamp with no clear maximum.

Figure 2 demonstrates another, related issue. Although not always the case, the timestamps that present difficulties in properly selecting the maximum value are often hovering at or below the instrument noise floor (0.15 nA). Observations near the instrument's sensitivity threshold are notoriously difficult to handle, as the true signal can be hard to extract. Moreover, maximum current values around this threshold often occur in tandem with inflated energy values. As energy has a direct relationship with spacecraft potential (see Equation(2)), very high energy values result in clearly erroneous spacecraft potential values, far above the automatic discharge threshold of the ISS (spacecraft potential of 40

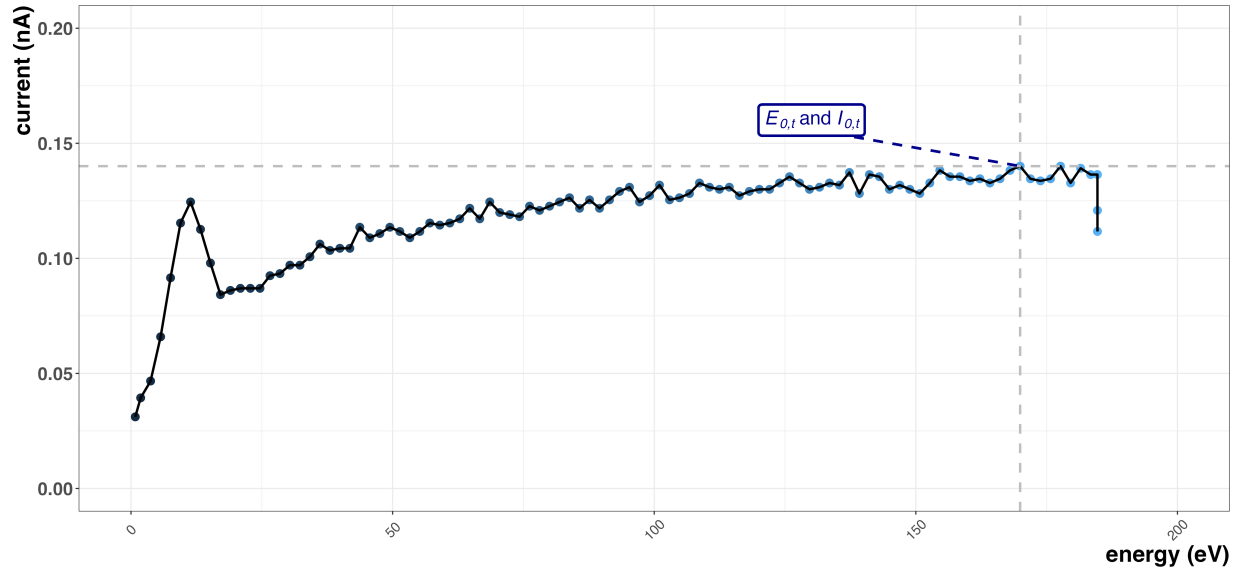


Figure 2: Empirical distribution of current values across energy bins for a single timestamp (2023-09-28 23:05:20 UTC). Energy bin is on the x-axis and current is on the y-axis (nA). The increase in energy value (eV) is represented through a lightening blue color palette, with indigo blues indicating lower energy values and azure blues indicating higher energy values. In this instance, choosing a maximum value is not clear, and the majority of observations fall in close proximity to the actual maximum.

volts) (Swenson et al. 2003). Initial thresholding efforts removed these points from consideration, creating a notable amount of missing data, particularly during the 7-hour overlap period used in cross-calibration efforts with FPMU.

Figure 3 shows the overlap period for Julian days 271-272 in 2023 for EPEE maximum current ( $I_{0,t}$ ) and energy ( $E_{0,t}$ ) values. Energy values are on the y-axis with time on the x-axis (month-day:hour) and colors pertaining to current values. All current values at or below the instrument noise floor (0.15 nA) are colored in dark grey, and the remaining current values (ranging from 0.15-5 nA) are represented with darker blues indicating lower values and yellows indicating higher values. Current values at or below the noise floor predominantly occur in tandem with very high energy values, as exemplified in Figure 2. Note that the initial respective energy value for the raw current maximum would be 169.9 eV, a clearly unphysical value.

Furthermore, when these data are aligned with sensors providing spacecraft potential observations from the FPMU instrument (Wide-Sweeping Langmuir Probe (WLP), Floating Potential Probe (FPP); please see Swenson et al. (2003) for more information on these sensors), more instances of missingness occur. Due to mismatching time stamps and missing data from FPMU, the already short window of time available for cross-calibration becomes further disjointed, limiting our ability to extract as much information as possible from the data. Typically, these values would be dropped from analysis but even seemingly erroneous observations may provide motivation for future explorations, thus we seek to preserve as many observations as possible.

For the remainder of the paper we consider an illustrative subset of data that overlaps with FPMU availability (Sept 28, 2023 22:00:00 UTC - Sept 29, 2023 05:00:00 UTC) to explore an alternative approach to handling noisy current input values, employing a series of techniques to capture data points previously considered unusable and smooth input values

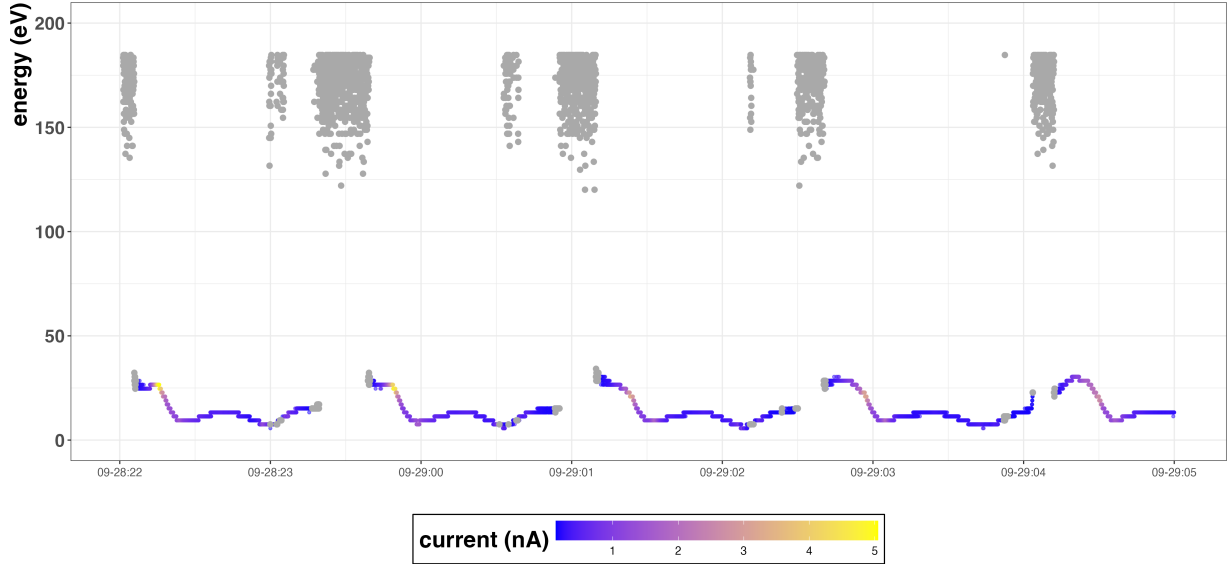


Figure 3: Maximum current values (y-axis) across time (x-axis), with colors indicating respective current values. Cooler colors indicate lower current values and warmer colors indicate higher current values (range 0-5 nA). All observations with current values at or below the instrument noise floor (0.15 nA) are colored in dark grey. These current values often - although not always - occur in tandem with very high energy values.

for use in the calculation of spacecraft potential. We show how this approach facilitates better cross-calibration with FPMU data and estimation of parameters crucial to mission safety and success.

## 2 Methods

### 2.1 Overview

As previously described, the instrument noise floor hovers around 0.15 nA, leading to mis-identification of the appropriate peak energy bin. An alternative approach to handling these values is outlined in the following steps:

1. Learn the smooth current surface: Fit Gaussian process (GP) models to the current

data  $\mathbf{I}$ , producing smooth estimates  $\mathbf{I}^S$  of the current surface as a function of time and energy.

2. Identify “minimal signal” timestamps: Using  $\mathbf{I}$ , identify a subset of times that are background-dominated  $\mathbf{t}^f = \{t_{k_1}^f, t_{k_2}^f, \dots, t_{k_M}^f\}$  with  $k_1, k_2, \dots, k_M$  indexing the selected timestamps.
3. Iteratively fit and refine noise profile: Consider the smooth current profile  $I_{k_m}^S(b)$  associated with time  $t_{k_m}$  across energy bins  $b \in \{1, \dots, 100\}$ . We model this profile as the sum of two main components: a Richards curve with a parabolic adjustment, which is our noise profile  $N_{k_m}^*(b)$  or “background”, plus a Gaussian impulse to capture “signal”. We do this for each profile, then select from these individual profiles to identify a conservative underlying noise floor profile  $N^*(b)$ .
4. Subtract the noise floor, post-process to ensure removal of any remaining noisy artifacts, and calculate downstream metrics: Let  $I^*(t, b) = I^S(t, b) - N^*(b)$  and let  $I^*$  denote the set of all smoothed, noise-floor-subtracted, cleaned current values. Using these  $I^*$  values in place of  $I$ , we can compute the maximum current value at timestamp  $t$  as  $I_{(0,t)}^*$  in order to better estimate the main parameters of interest (e.g. spacecraft potential).

Figure 4 shows a different perspective of these steps, with inputs (teal blue rectangles), outputs (burnt orange rectangles) and processes (plum circles) showing movement from observation-based input to the derived variables of interest (white box with black outline).

Although specific decisions have been made at various steps that were best-suited to these data and application, the overall methodology represents a general denoising approach. For example, in Step 1 we implement a Vecchia approximation in the GP to address computational challenges with the data volume; a different GP approximation could easily replace

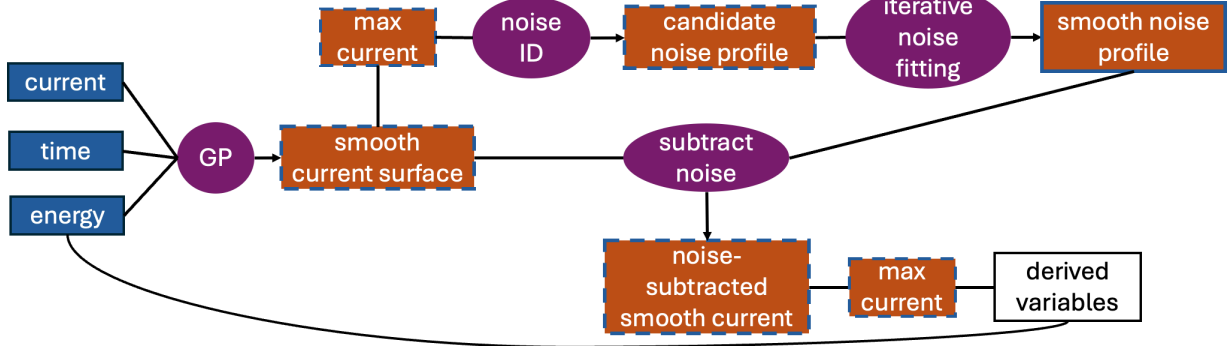


Figure 4: Flowchart depicting the methodology for handling values near the instrument noise floor. Inputs are in blue and outputs in burnt orange, both are rectangular shapes. Outputs that then become inputs in subsequent steps have a dashed outline. Processes are in purple circles with a solid line representing input to a process and an arrow representing output of a process. The final, desired variables of interest are identified with a white box outlined in black.

scaled Vecchia or - depending on the size of the data - an exact GP could be implemented. The noise floor itself could be described with a known shape (e.g. a constant offset), if this were appropriate, instead of learning this profile from the data.

## 2.2 Step 1: Fit a smooth surface using a GP approximation

Initially, the data are subset into quarter-days before processing with the goal of reaching a balance between under- and over-smoothing the current surface, and to facilitate the ability to handle edge cases of noise behavior. To smooth the current surface over time and energy, we use a Gaussian process (GP). Gaussian processes are flexible statistical models that allow for surfaces to be fit to data without requiring many assumptions to be made about the surface structure. GPs can be conceptualized as distributions over functions (or surfaces) or as infinite-dimensional generalizations of the multivariate Gaussian distribution. GPs are fully specified by two functions, a mean function ( $m : \mathbf{X} \rightarrow \mathbb{R}$ ) and a covariance

function ( $k : \mathbf{X} \times \mathbf{X} \rightarrow \mathbb{R}^+$ ). The mean function is commonly set to zero for centered data, leaving the learned covariance structure between observations to drive the model’s behavior. The current surface over time and energy is then defined:

$$I(x_i) = I^S(x_i) + \epsilon_i, \quad I^S(x_i) \sim GP(0, k(\cdot)), \quad \epsilon_i \sim N(0, \sigma^2) \quad (3)$$

Let  $x_i = (t_i, e_i)$  denote the time/energy combination associated with an observation. Then, the vector  $\mathbf{I} = (I(x_1), \dots, I(x_n))^T$  of responses at  $n$  input values  $x_1, \dots, x_n$  follows an  $n$ -variate Gaussian distribution with covariance matrix  $K$ ;  $k(\cdot)$ , the  $(i, j)$ th entry of  $K$ , describes the covariance between current observations  $i$  and  $j$  as a function of the corresponding time/energy combinations (Betancourt 2020, Lawrence et al. 2022). We define  $k(\cdot)$  as a Matern 3/2 kernel (Rasmussen & Williams 2006) function, with length scale and process variance parameters of the kernel (i.e., the parameters that specify how “wiggly” the surface is and how far it tends to stray from its mean), along with noise variance  $\sigma^2$ , optimized via maximum likelihood.

Inverting the covariance matrix in the likelihood computation becomes infeasible as  $n$  increases due to the necessary  $O(n^3)$  operation. Many approaches have been developed to circumvent this issue. Once such approximation, the Vecchia approximation (Vecchia, 1988), was long popular in spatial statistics and has seen much recent extension work. Here we follow the methodology of Lawrence et al. (2022), who adapt approaches from spatial statistics to present a highly scalable algorithm that “enabl(es) ordering, neighbor-search, estimation and joint prediction and simulation in near-linear time” (Lawrence et al. 2022).

### 2.3 Step 2: Identify noise and create a noise profile

To identify timestamps that are noise-dominated (i.e., lack a discernible maximum value, see Figure 2), we leveraged the understanding that maximums identified in energy bins

above a certain threshold result in non-physical spacecraft potential values. We assume that maximum currents identified in bins 50-100 are likely instances of noise. After flagging likely noise timestamps, the next step is to isolate those that represent background only conditions. To achieve this, the algorithm leverages the clustering of likely noise times, visually evident in Figure 6 as dense groups of observations at higher energy values. This heuristic approach focuses on identifying the "heart" of these observations, targeting the central regions where noise dominance is most pronounced. For identified noise timestamps, the algorithm evaluates the total decrease in current across the first 20 energy bins, which should be zero for background-only profiles. A rolling window is then applied to enforce monotonicity in the lower energy bins, iteratively expanding the window size until a sufficient number of timestamps meet the zero-decrease criterion. This ensures that the selected timestamps represent the most stable and minimal signal possible. By isolating a predefined percentage (default 10%) of the flagged times, the algorithm effectively captures background conditions while avoiding outliers or transitional states, enabling accurate characterization of the instrument's baseline noise behavior.

After identifying background timestamps, we separate each background-dominated current profile  $I_{k_m}^S(b)$  into instrument baseline and ionospheric signal and apply a profile-fitting procedure that models the noise floor as the sum of three components: a Richards curve, a parabolic curve, and a Gaussian peak.

$$I_{k_m}^S(b) \approx \underbrace{f_{k_m,R}(\theta_R) + f_{k_m,P}(\theta_P)}_{\text{instrument baseline}} + \underbrace{f_{k_m,G}(\theta_G)}_{\text{ionospheric signal}} \quad (4)$$

where the instrument baseline is composed of the Richards curve fit ( $f_{k_m,R}(\theta_R)$ ) and parabolic component ( $f_{k_m,P}(\theta_P)$ ), parameterized by  $\theta_R = (A, k, x_0, \nu, A_0)$  and  $\theta_P = (p, q, r)$ , respectively. Any remaining structure is identified using a Gaussian peak ( $\theta_G = (\alpha, \mu, \sigma)$ ), with parameters  $\theta_G = (\alpha, \mu, \sigma)$  (see Appendix X for details).

The Richards curve is a generalization of the logistic function that introduces a shape parameter  $\nu$  to allow for asymmetry in the sigmoidal form. Although originally developed for growth modeling in biology, epidemiology, and ecology (Richards 1959), it is well suited to modeling the stabilizing behavior of instrument noise across energy bins, capturing smooth rises and plateaus with flexibility in slope and curvature. As such, the Richards component is always included as the base model in our noise floor estimate.

After subtracting the Richards fit, a Gaussian component is fit to the residuals to capture any remaining localized structure. This structure is presumed to represent true signal rather than background, so the Gaussian is used only during fitting and not added to the final noise floor. Once parameter estimates for the Richards and Gaussian components have stabilized, a parabolic term is introduced to model low-order curvature not captured by the sigmoid. Thus our refined noise floor profile for each timestamp becomes  $N_{k_m}^*(b) = f_{k_m,R}(\theta_R) + f_{k_m,P}(\theta_P)$  (see Appendix 6 for further details and visualizations).

Finally, among all candidate noise profiles, the one with the smallest integral over energy bins 2 through 20, found to be a stable region over which to select the noise profile, is used as the final estimate.

Figure 5 shows results for the first and fourth quarters of Julian day 271 (both with  $n=10799$ ) with GP-smoothed current values (y-axis) for each timestamp plotted across energy bins (x-axis) and color indicating energy value. There are 100 timestamps identified as 'likely minimal signal' from each period. After each timestamp undergoes the fitting process individually, the fitted noise profile with the smallest integral is selected (highlighted in red). The first quarter (top facet) candidate selection does a fairly good job and little Gaussian shape is left in the residuals to fit and remove. In contrast, the initial candidate selection in the fourth quarter (bottom facet) picks up signal in the earlier bins, which we successfully capture through the iterative fitting process and preserve by

subtracting this shape from the final fitted noise profile.

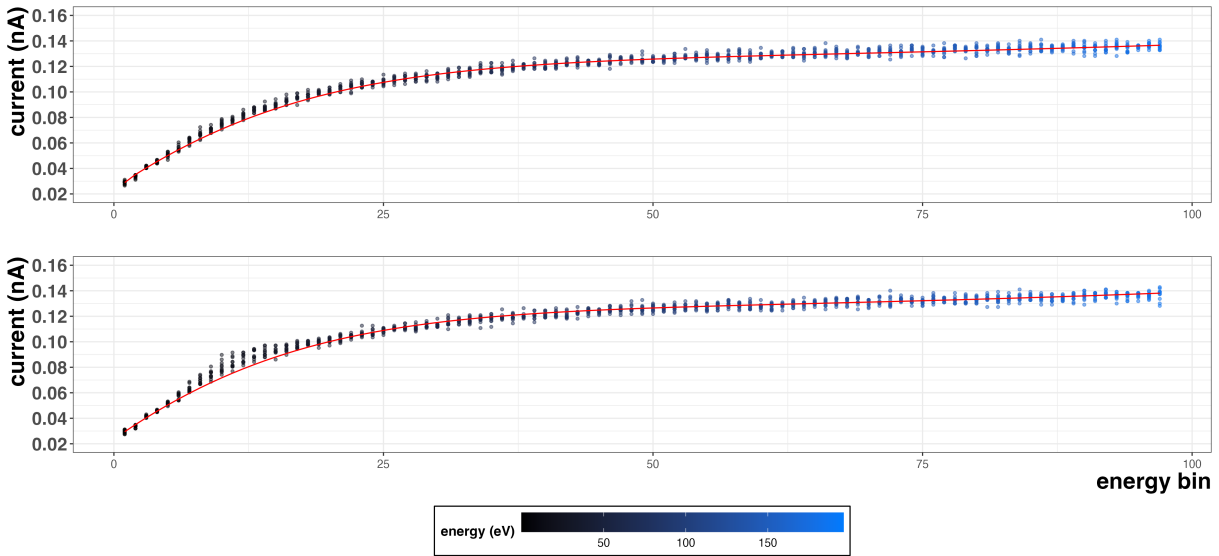


Figure 5: Results of the noise profile fitting process for the first (top facet) and fourth quarter (bottom facet) of Julian day 271 (both with  $n=10799$ ). Candidate noise timestamps (those identified as likely minimal signal) are plotted across energy bins (x-axis) and GP-smoothed current values (y-axis) with raw energy identified by coloring (blues lightening with increasing values). The final fitted noise profile, comprised of Richards and parabolic component shapes, is highlighted in red.

## 2.4 Step 3: Learn the smooth current profile

Because the noise floor is omnipresent, we subtract it from our predicted GP fit to yield a learned current surface that is smoother (due to the GP) and less dominated by instrument noise in low-current times (due to the background identification and subtraction). The noise-subtracted, smooth current surface is then used to select the maximum current value by timestamp and the respective energy value from the raw energy values is identified. These maxima represent the inferred peak signal locations and are the only non-constants that enter into the equation for calculating our main downstream metric of interest, space-

craft potential (Equation (2)).

## 2.5 Step 4: Post-processing

Although the noise-fitting process effectively removes the majority of background variation across the 13-month dataset, several post-processing filters are applied to address outlier cases and ensure robust signal identification. Specifically, we remove time intervals that exhibit prolonged sequences of high-energy maxima, which often indicate instrumental anomalies or solar interference. We also exclude observations in which the peak bin undergoes a sudden and drastic downward shift, suggesting an artifact introduced during noise floor subtraction, particularly after timeline merging. Finally, any maxima associated with energy values exceeding 45 eV are discarded, as these are considered physically implausible in the context of this analysis. All removed entries are flagged and retained in the final dataset to preserve transparency and support further exploration.

# 3 Verifications

## 3.1 Noise Floor Identification and Modeling

Figure 6 shows maximum energy value ( $E_0$ ) results for the 7-hour period spanning Julian days 271-272. Smoothed, noise-subtracted current values are depicted with darker blues indicating lower values and yellows indicating higher values. Time is on the x-axis. Observations identified as noise and dropped through the original thresholding methodology are colored in gray. The black points represent observations that were statistically indistinguishable from zero (at  $\alpha = 0.05$  confidence level) through the alternative methodology and are thus considered “true noise”. The revised approach results in a markedly lower number of points classified as noise (38 versus 2,144 with the original method), substantially

increasing the amount of usable data for characterizing plasma behavior.

Furthermore, the observations identified as “true noise” now predominantly occur in a small window of time, latitude and longitude (further described in Figure 8). Although careful consideration over the entire 13 months is still needed, observations flagged as ‘true noise’ through the new methodology may serve as a starting point for identification of the location of the Equatorial Ionization Anomaly. This is an exciting possible direction of future research.

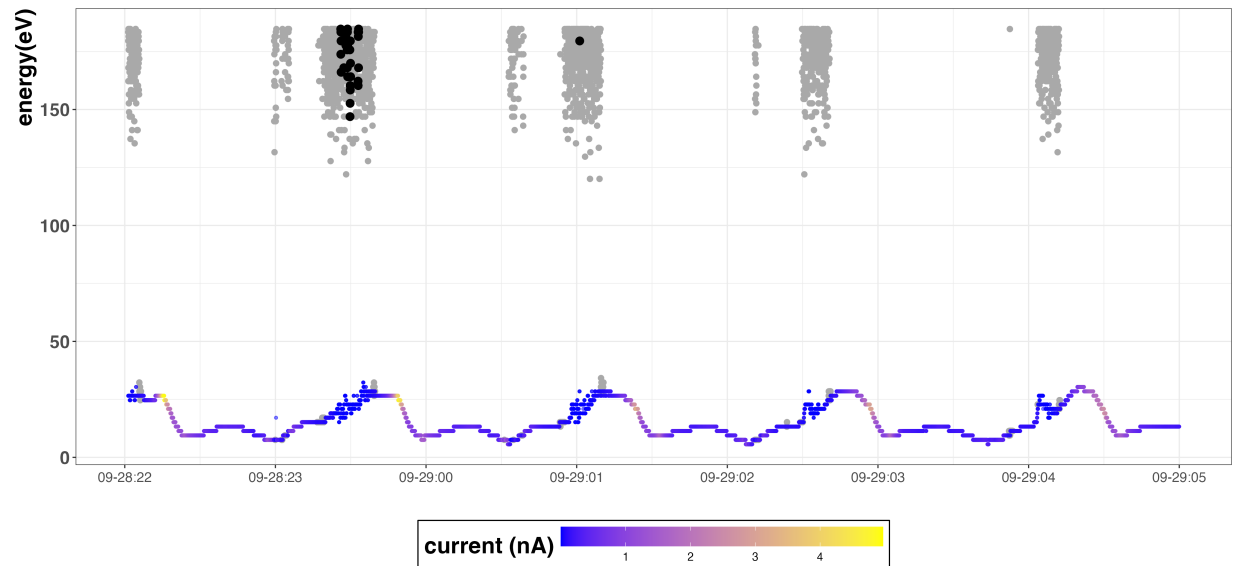


Figure 6: Comparison of original and new methodologies for handling noisy current values. Observations chosen using the new methodology are colored by the noise-subtracted, smoothed current value with points identified as statistically indistinguishable from zero (‘true noise’) in black. Original methodology results for observations that were considered noise and removed from consideration are in grey.

### 3.2 Spacecraft Charge Over Time

Figure 7 below demonstrates the increased data availability for calibration with FPMU instrument data (FPP and WLP) after implementing the new methodology. In even a

seven-hour period, notable gaps exist when using the original methodology, making interpolation between periods of available data difficult (top panel). The smoothed current values offer more information about spacecraft charging values during these time periods, in some instances even offering information missing from FPMU observations. These results establish a foundation for better estimates of the more complex variable plasma density, which involves calibration between the FPMU and EPEE instruments.

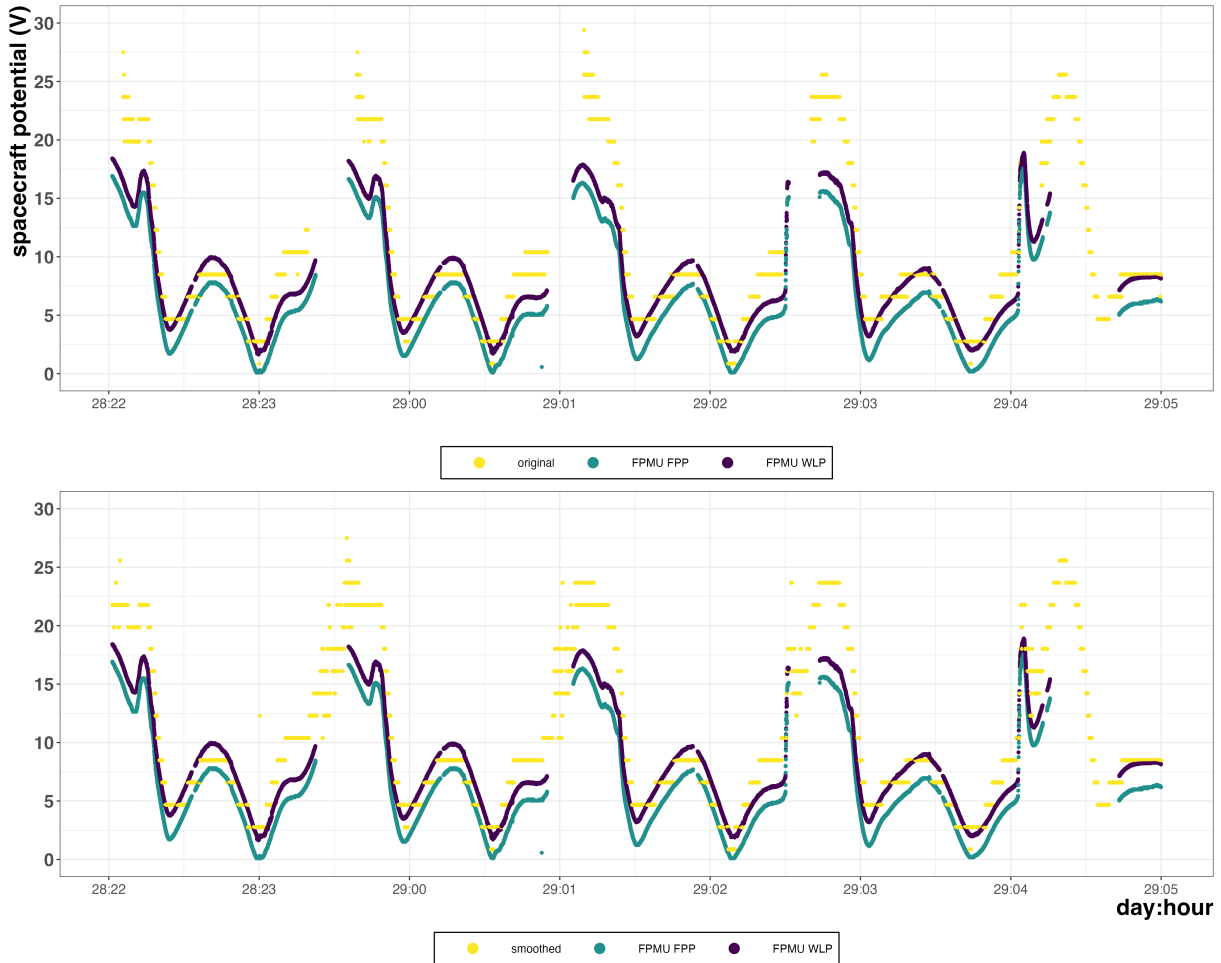


Figure 7: Spacecraft potential estimation results for both the original (top panel) and alternative (bottom panel) methods compared to estimates from the WLP (mulberry) and FPP (chartreuse) sensors on the FPMU instrument. Both original and smoothed results are in dandelion; the x-axis shows the seven hours between Julian days 271-272 shared by the two sensors in 2023.

## 4 Conclusion

### 4.1 Potential applications

This methodology, although specific to these data and scenario, provides a general framework applicable to other sensor interpretation tasks. Both the pipeline and the resulting smoothed energy and current surfaces can be used in the next steps of our work, which include plasma density estimation, exploration of the EIA in relation to spacecraft charging and density values, and analysis of the fluctuation of these variables in relation to the ISS orbit. These estimates also have the potential for integration to output from the International Reference Ionsphere (IRI) model. The IRI is considered the source of truth for data describing the physical parameters of the ionosphere and as of 2014 is the International Standardization Organization standard for the ionosphere ([Bilitza et al. 2022](#)). As the IRI is an empirical, data-based model, possible disadvantages arise during novel conditions. For example, during anomalous periods in the solar cycle that may not have been previously recorded, such as the very low solar cycle minimum in 2008-2009, the IRI can sometimes over- or underestimate physical parameters. In this instance, this misalignment was identified by several research groups and the IRI model was corrected ([Bilitza et al. 2022](#)). As the EPEE instrument provides data during part of Solar Cycle 25 as it heads towards the solar maximum ([Maldonado et al. 2023](#)), observations could serve to validate - and if necessary - possibly calibrate the IRI model in service to the scientific community.

Due in large part to this novel application of statistical methods to signal processing, we have identified the potential for 'true' noise to be used as an indicator of physical phenomena. Figure 8 displays spacecraft potential estimates for the original data (grey) and with implementation of the new method (black) against the backdrop of latitude (y-axis) and longitude (x-axis) taken from GPS aboard the ISS. Previously, observations

identified as noise did not exhibit a particular pattern, showing some scattering across locations. Now, all observations identified as noise ( $n=38$ ) are concentrated within a very small latitude range, suggesting these observations may not be random. Although not pictured here, initial exploration across the entire dataset showed true noise occurring in a similar spatial range. Further exploration over a longer timeline with confounding factors taken into consideration is needed.

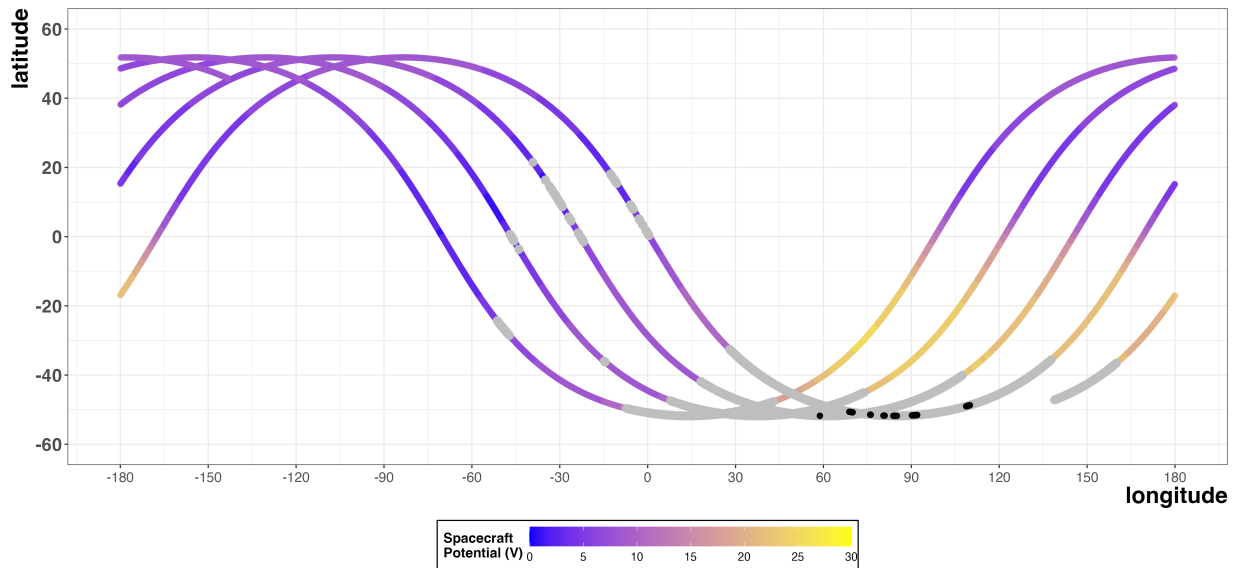


Figure 8: Spacecraft potential (V) in blue fading to yellow with increasing values are plotted across longitude (x-axis) and latitude (y-axis) for the 7-hour case study time period. The relatively small number of 'true noise' values ( $n=38$ ) occur in a very concentrated latitude range and are colored in black. Previous thresholding of current values under the noise floor are in gray and show much more considerable spatial spread.

## 4.2 Future Directions and Considerations

Code used to process the 7-hour time period used as an example throughout this paper has been formatted to allow for batch processing across the 13-month dataset. Excitingly, our team has now implemented the non-trivial code alterations necessary to allow for

heteroskedastic noise consideration within the scaled Vecchia GP approximation. Although the paper explaining these methods and subsequent ramifications is in preparation (Potter et al. 2025), we are ready to explore implementation for EPEE data and to compare to homoskedastic noise assumptions.

Cross calibration to the FPMU data is ongoing as part of a full data release effort by the team. This work includes a thorough review of the modified algorithms recently presented for the WLP instrument, intended ”to yield improvements in the quality of the plasma density, temperature, and potential parameters extracted from the probe data” (Minow et al. 2023).

## 5 Disclosure statement

The authors declare that no conflicts of interest exist. Research presented in this manuscript was supported by the Laboratory Directed Research and Development (LDRD) program of Los Alamos National Laboratory (LANL) under project No. 20240045DR. Work at LANL is conducted under the auspices of the United States Department of Energy. The authors also acknowledge the support of the Department of Defense (DoD) Space Test Program which provides mission design, spacecraft acquisition, integration, launch and on-orbit operations support for DoD’s science and technology (S&T) experiments, and manages all DoD payloads on the International Space Station. Approved for public release: LA-UR-25-29600.

## 6 Data Availability Statement

The data and code used in this paper have been made available at the following URL: XX.  
\*\*Note: Data have been reviewed by our organization and released for public access. The

code release is in progress. As soon as it is approved we can make public the git repository containing both.\*\*

## SUPPLEMENTARY MATERIAL

The supplementary material contains two figures that further describe the iterative noise profile fitting process. Figures 9 and 10 both describe the selected noise profile with the smallest integral out of the candidate noise profiles for the first quarter of Julian day 272. Figure 9 plots the individual components that constitute the refined noise floor profile (Richards and parabolic curves) and identified true signal (Gaussian shape). Raw initial input and the final fitted profile (Richards and parabolic input combined) are also displayed. Figure 10 displays the respective parameter estimates for each of these components (Richards, parabolic, Gaussian shapes) in table form. Parameters for each shape that convey the most information about the importance of the shape in the final profile fit are highlighted in colors matching the plot. These include Richards A (point of inflection), Gaussian amplitude, and the three parabolic components (quadratic term (p), slope (q), intercept (r)).

### **Noise floor decomposition with raw signal.**

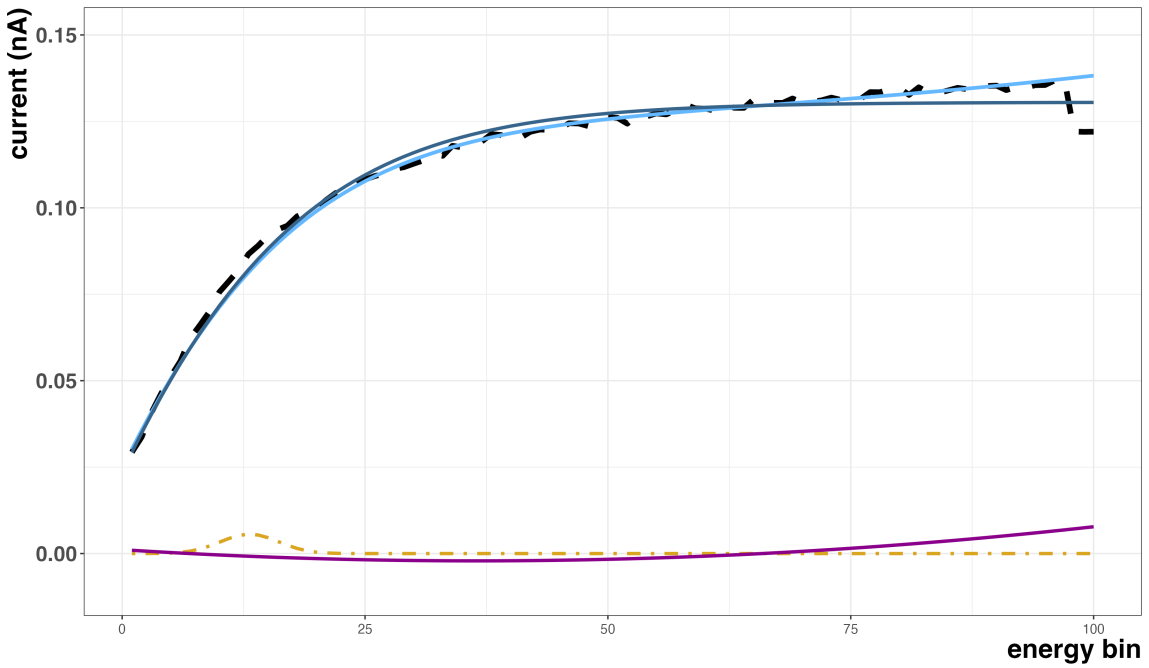


Figure 9: Components of the noise profile fitting process for the first quarter of Julian day 272 ( $n=10799$ ). The selected noise profile from all candidate noise timestamps is decomposed into Richard's fit (steel blue), parabolic (magenta) and remaining Gaussian signal (mustard). Raw signal is in dotted black and the final fitted noise profile is in cornflower blue. Energy bin is on the x-axis and current (nA) is on the y-axis.

#### Parameter estimates for noise floor components.

	parameter	estimate
<b>A</b>	<b>Richards A</b>	<b>13.656123</b>
<b>k</b>	Richards k	0.080291
<b>x0</b>	Richards $x_0$	0.646444
<b>nu</b>	Richards v	91.056505
<b>A0</b>	Richards $A_0$	-13.525871
<b>amp</b>	<b>Gaussian amplitude</b>	<b>0.013125</b>
<b>mu</b>	Gaussian $\mu$	11.580737
<b>sigma</b>	Gaussian $\sigma$	3.000000
<b>p</b>	<b>Parabola p</b>	<b>0.000003</b>
<b>q</b>	<b>Parabola q</b>	<b>-0.000186</b>
<b>r</b>	<b>Parabola r</b>	<b>0.001193</b>

Figure 10: Parameter estimates of the noise profile fitting process for the first quarter of Julian day 272 (n=10799) after convergence. The main parameter estimates of interest are highlighted in colors corresponding to 9. Richard's A (steel blue) describes the max height at the inflection point. A relatively large value suggests that this shape dominates in the noise fitting process. The parabolic parameters (magenta) are hovering near zero, suggesting that they do not manipulate the fit much. Remaining Gaussian signal (mustard) is mainly described by amplitude, with small values indicating that little true signal remains after the Richards and parabolic iterative fitting.

## References

Betancourt, M. (2020), ‘Michael betancourt, phd’.

**URL:** <https://betanalpha.github.io/>

Bilitza, D., Pezzopane, M., Truhlik, V., Altadill, D., Reinisch, B. W. & Pignalberi, A. (2022), ‘The international reference ionosphere model: A review and description of an ionospheric benchmark’, *Reviews of Geophysics* **60**(4), e2022RG000792.

**URL:** <https://doi.org/10.1029/2022RG000792>

Hastings, D. E. (1995), ‘A review of plasma interactions with spacecraft in low earth orbit’, *Journal of Geophysical Research: Space Physics* **100**(A8), 14457–14483.

**URL:** <https://doi.org/10.1029/94JA03358>

Howard, J. (2002), Kinetic theory, in ‘Introduction to Plasma Physics’, Australian National University, Canberra, Australia, chapter 2. Accessed on: December 4, 2024.

**URL:** <https://people.physics.anu.edu.au/jnh112/AIIM/c17/chap02.pdf>

Lawrence, E., Guinness, J. & Katzfuss, M. (2022), ‘Scaled vecchia approximation for fast computer-model emulation’, *SIAM/ASA Journal on Uncertainty Quantification* **10**(2), 537–554.

Maldonado, C. A., Ketsdever, A. D., Balthazor, R. D., Neal, P. C., Wilson, G. R., Williams, J. D. & McHarg, M. G. (2023), ‘Automated plume sentry observations during international space station thermal control system venting’, *Journal of Spacecraft and Rockets* **60**(1), 339–350.

**URL:** <https://doi.org/10.2514/1.A34995>

Maldonado, C. A., Ulrich, R., Moran, K., Potter, K., Castro, L., Lira, P. A. R., Eddy, T., Klem, S. M., Janhunen, J., Delzanno, G. L., McGlown, J., Weaver, B., Balthazor, R., Williams, J. D. & McHarg, M. G. (2025), Initial on-orbit results from the electric

propulsion electrostatic analyzer experiment (EpEe), in ‘AIAA SciTech 2025 Forum’.

**URL:** <https://arc.aiaa.org/doi/10.2514/6.2025-2547>

Minow, J. I., Debchoudhury, S., Barjatya, A., Coffey, V. & Parker, L. N. (2023), Floating potential measurement unit (fpmu) data processing algorithm development and analysis assessment, Technical Memorandum NASA/TM-20230013386, NASA Engineering and Safety Center. Accessed on: December 4, 2024.

**URL:** <https://ntrs.nasa.gov/api/citations/20230013386/downloads/20230013386.pdf>

Minow, J. I., Jordanova, V. K., Pitchford, D., Ganushkina, N. Y., Zheng, Y., Luca Delzanno, G., Jun, I. & Kim, W. (2024), ‘ISWAT spacecraft surface charging review’, *Advances in Space Research* .

**URL:** <https://www.sciencedirect.com/science/article/pii/S0273117724008822>

Potter, K., Moran, K., Ulrich, R., Castro, L., Stenning, D., Bingham, D. & Maldonado, C. (2025), ‘Scalable heteroskedastic gaussian process models for large inhomogeneous data’, Manuscript in preparation.

Rasmussen, C. E. & Williams, C. K. I. (2006), *Gaussian Processes for Machine Learning*, MIT Press, Cambridge, MA.

**URL:** <https://gaussianprocess.org/gpml/>

Richards, F. J. (1959), ‘A flexible growth function for empirical use’, *Journal of Experimental Botany* **10**(2), 290–301.

Swenson, C. M., Fish, C. S. & Thompson, D. C. (2003), Calibrating the floating potential measurement unit, in ‘Proceedings of the 8th Spacecraft Charging Technology Conference’, Huntsville, Alabama.